Electronic and magnetic properties of the candidate magnetocaloric-material double perovskites La_2MnCoO_6, La_2MnNiO_6, and La_2MnFeO_6

C. Gauvin-Ndiaye,[1] T. E. Baker,[1] P. Karan,[1] É. Massé,[1] M. Balli,[1] N. Brahiti,[1] M. A. Eskandari,[1] P. Fournier,[1,2] A.-M. S. Tremblay,[1,2] and R. Nourafkan[1]

[1]*Institut quantique, Département de Physique and RQMP, Université de Sherbrooke, Sherbrooke, Québec, Canada J1K 2R1*
[2]*Canadian Institute for Advanced Research, Toronto, Ontario, Canada M5G 1Z8*

(Received 26 July 2018; published 17 September 2018)

The search for room-temperature magnetocaloric materials for refrigeration has led to investigations of double perovskites. In particular, a puzzle has appeared in the La_2MnNiO_6, La_2MnCoO_6, and La_2MnFeO_6 family of compounds. They share the same crystal structure, but while La_2MnNiO_6 and La_2MnCoO_6 are ferromagnets below room temperature, La_2MnFeO_6, contrary to simple expectations, is a ferrimagnet. To solve this puzzle, we use density functional theory calculations to investigate the electronic structure and magnetic exchange interactions of the ordered double perovskites. Our study reveals the critical role played by local electron-electron interaction in the Fe-d orbital to promote the Fe^{3+} valence state with half-filled d shell over Fe^{2+} and to establish a ferrimagnetic ground state for La_2MnFeO_6. The importance of Hund's coupling and Jahn-Teller distortion on the Mn^{4+} ion is also pointed out. Exchange constants are extracted by comparing different magnetically ordered states. Mean field and classical Monte Carlo calculations on the resulting model give trends in T_C that are in agreement with experiments on this family of materials.

DOI: 10.1103/PhysRevB.98.125132

I. INTRODUCTION

The magnetocaloric effect leads to an increase of the temperature when certain materials are exposed to a magnetic field and decreases when they are removed from it. In order to be suitable for room-temperature magnetic refrigeration, magnetocaloric materials need to exhibit a large change in magnetization around room temperature. The most interesting materials for this technology are hence ferromagnets with a high total moment per formula unit that undergo a magnetic phase transition to a paramagnetic state at room temperature [1]. Recently, double perovskites have been given considerable attention for this technology because of the low-production cost, stronger spin-phonon interactions, higher chemical stability, and better insulating properties.

Double perovskites La_2MnNiO_6 (LMNO) and La_2MnCoO_6 (LMCO) exhibit near room-temperature ferromagnetism, with a Curie temperature of $T_C \simeq 280$ K [2] and $T_C \simeq 226$ K [3], respectively. From a practical point of view, LMNO has a refrigerant capacity similar to that of gadolinium [4] and would be a promising candidate for magnetocaloric refrigeration if one could increase its Curie temperature through chemical substitution or thermal treatment. The low-temperature valence states of Mn and Ni ions in La_2MnNiO_6 are tetravalent (Mn^{4+}) and divalent (Ni^{2+}), with magnetic moments of $3\mu_B$ and $2\mu_B$, respectively, for a total of $5\mu_B$ per formula unit (f.u.) [5]. LMCO is also a ferromagnet with tetravalent Mn and divalent Co and a total moment of $6\mu_B$/f.u.

This motivates the study of La_2MnFeO_6 (LMFO): naively, one may think that substituting Ni or Co with Fe may increase T_C since Fe has a magnetic moment of $5\mu_B$ in its trivalent high-spin configuration, i.e., Fe^{3+} with half-filled d shells. Ferromagnetic LMFO with trivalent Mn and Fe would then have a higher total moment ($9\mu_B$/f.u.) and possibly a higher Curie temperature than both LMCO and LMNO. However, experimental results show that LMFO is a ferrimagnet with antiparallel moments on neighboring Mn and Fe sites [6–8].

The difference in the ground-state magnetic orders in LMFO and LMNO/LMCO is puzzling because all of these materials share the same crystal structure. The resulting double-perovskite $A_2B'B''O_6$ structure stems from the perovskite structure ABO_3 where half of the transition-metal sites (B) are occupied by Mn ions and the other half by Ni, Fe, or Co ions [9]. In such a structure resulting from the solid solution of $AB'O_3$ and $AB''O_3$, the interaction between neighboring moments occurs through the oxygen-mediated superexchange interaction. Superexchange facilitates hopping of the electrons from the oxygen p shells to the magnetic ions d shell, leading to a reduction of the total energy due to a kinetic energy advantage. It can be antiferromagnetic (AFM) or ferromagnetic (FM), depending on structural parameters such as the B'-O-B'' bond angle and the B'-O-B'' bond length. Furthermore, crystal-field splitting, Hund's coupling, and onsite electron-electron repulsion can also influence the superexchange interaction. The roles played by the latter parameters depend on the d-shell occupancy.

Finally, the properties of double perovskites are strongly influenced by the level of cationic order. In the ordered phase, the $3d$ metal cations crystallize in the so-called rocksalt structure in which Mn and Ni (Fe, Co) atoms occupy alternate positions in each spatial direction. In the pristine double perovskites, the space-group symmetry becomes $P2_1/c$ [3,4,10]. In the disordered phase, for which not only B'-O-B'' but also B'-O-B' and B''-O-B'' bonds are present, the materials have

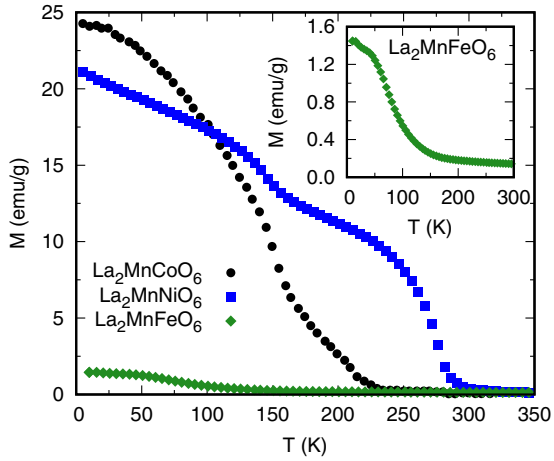

FIG. 1. Magnetization as a function of temperature in bulk La_2MnCoO_6 (black circles), La_2MnNiO_6 (blue squares), and La_2MnFeO_6 (green triangles). Inset: zoom on the magnetic transition in LMFO.

been reported to crystallize in the *Pbnm* space group [3,4,11]. For example, in La_2MnCoO_6, the ferromagnetic Mn-O-Co bonds are diluted in a matrix of antiferromagnetic Co-O-Co and Mn-O-Mn bonds. Depending on the growth parameters, we measure two distinct transitions in a bulk sample as shown in Fig. 1 for La_2MnCoO_6 and La_2MnNiO_6, demonstrating a mixture of the ordered and the disordered domains. Tuning the growth parameters allows us to tune the proportion of both phases and eventually to remove completely the low-temperature transition associated to the cation-disordered phase and leaving only the high-temperature transition of the cation-ordered phase [12]. In the present theoretical study, we will focus on the magnetic properties of the cation-ordered phase while trying to explain the absence of a high-temperature transition in La_2MnFeO_6 as shown also in Fig. 1.

The understanding of the microscopic mechanisms at play in LMFO could lead to the design of new materials that could be more suitable for magnetic refrigeration than LMNO and LMCO.

We first investigate the ground states of LMNO, LMCO, and LMFO with density functional theory (DFT) calculations in Sec. II. We compare the structural, electronic, and magnetic properties of the three materials in order to understand the impact of electron-electron interaction and structural distortion on the ground state of LMFO. In Sec. III, electronic structure calculations for different types of magnetically ordered ground states allow us to extract exchange coupling constants and corresponding mean-field transition temperatures. In Sec. IV, we improve the estimates of the Curie temperature using Monte Carlo calculations. The method specific to each section is described in the opening subsection.

II. ELECTRONIC STRUCTURE FOR La_2MnNiO_6, La_2MnCoO_6, and La_2MnFeO_6

We first describe the method, then present results for LMNO and LMCO in Sec. II B. The puzzling case of LMFO is presented in Sec. II C.

A. Method

The GGA($+U$) calculations are performed within the full-potential all-electron basis set as implemented in the WIEN2K code, using the Perdew-Burke-Ernzerhof (PBE) functional [13]. In the GGA $+ U$ calculation, the effective interaction $U_{eff} = U - J$ has been set to 3.0 eV for Mn, Ni, Co, and Fe d orbitals (except when specified otherwise in the text). We use the GGA $+ U$(SIC) method with an approximate correction for the double counting [14]. Structure optimization is performed on LMNO, LMCO, and LMFO using the $P2_1/c$ space group. In order to confirm the ground-state magnetic order, structure optimization is performed using two different magnetic alignments of Mn and Fe moments: ferromagnetic (FM) and (G-type) antiferromagnetic (AFM). A plane-wave cutoff of $R_{\rm mt}K_{\rm max} = 8.1$–$8.3$ and a **k** mesh of 50 points in the Brillouin zone are used for self-consistent calculations presented in Secs. II B and II C. We check the convergence with respect to the number of **k** up to 250 points in the irreducible Brillouin zone and to $R_{\rm mt}K_{\rm max}$ cutoff up to 8.1 for LMNO and LMCO, and 8.3 for LMFO. In supercell calculations, a $R_{\rm mt}K_{\rm max} = 7$ and 60 k points were used (Sec. III).

B. La_2MnNiO_6 and La_2MnCoO_6

Starting with La_2MnNiO_6, our *ab initio* electronic structure calculations confirm that the orbital occupancy of Mn-d and Ni-d are very close to the nominal ones. The oxidation state of Mn and Ni are Mn^{4+} and Ni^{2+} with $3d^3_\sigma d^0_{\bar\sigma}$ and $3d^5_\sigma d^3_{\bar\sigma}$ electronic configurations, where $\bar\sigma = -\sigma$. Hence, the predicted total magnetic moment is $\simeq 5\mu_B$/f.u., which is in good agreement with experimental data [4]. The energy difference between AFM and FM configurations is 0.13 eV/f.u. in GGA calculations, and 0.16 eV/f.u. in GGA $+ U$ calculations. Figures 2(a) and 2(d) show partial density of states (DOS) of LMNO calculated from GGA and GGA $+ U$ methods, respectively. The calculation is done in a FM magnetic moment configuration. Partial DOS of up (down) component is denoted by positive (negative) value. Both methods predict an insulating ground state. Although the charge gap increases between GGA and GGA $+ U$ calculations, the partial charge occupations and the magnetic moments of the transition-metal ions do not depend sensitively on effective Coulomb interaction. The overlap between partial DOS of transition metal and oxygen above the Fermi level indicates which virtual hopping processes can be realized in the system. The partial DOS above the Fermi level illustrates good overlap between Ni-e_g and O-p, in particular for down spin. Similarly, Mn-e_g up and O-p partial DOSs overlap well above the Fermi level. The optical gap predicted by GGA calculations is around 0.8 eV and, above the Fermi level, the states are dominated by the Mn-e_g orbitals, as shown in Fig. 2(a). Including the electron-electron interaction through GGA $+ U$ calculation pushes the Mn-e_g states to higher energies, hence, just above the Fermi level, the states become dominated by the O-p orbitals. The charge gap also increases to 1.7 eV, as shown in Fig. 2(d).

In LMNO, the main factor determining the ground-state magnetic structure is the kinetic energy gain due to superexchange interaction. This is illustrated schematically in Fig. 2(g) where the position of the atomic levels roughly

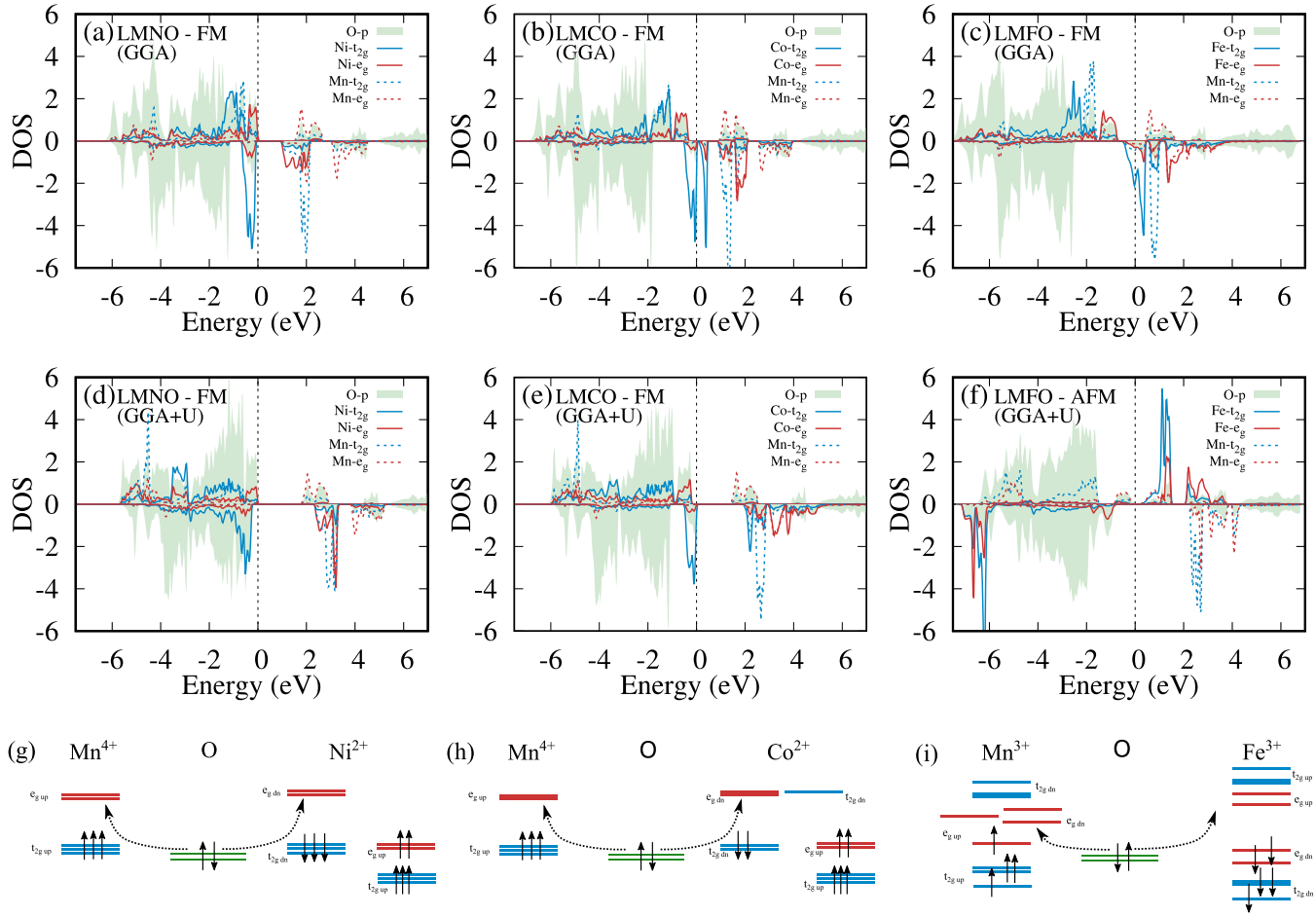

FIG. 2. Spin-resolved partial density of states for Mn-e_g, Mn-t_2g, Ni (Co, Fe)-e_g, Ni (Co, Fe)-t_{2g}, and O-p from GGA calculations (top row) and GGA + U (middle row) calculations. GGA + U calculations are performed with $U_{eff} = 3$ eV. The upper part in each panel is majority-spin DOS result, and the lower the minority-spin one. GGA calculations predict an insulating ferromagnetic ground state for (a) LMNO and (b) LMCO, and a metallic ferromagnetic ground state for (c) LMFO. GGA + U calculations predict an insulating ferromagnetic ground state for (d) LMNO and (e) LMCO, and an insulating ferrimagnetic ground state for (f) LMFO. Bottom row: schematic representation of the superexchange interaction in (g) LMNO, (h) LMCO, and (i) LMFO. The figures represent schematically the weight of each orbital with respect to the others and are derived from the partial DOS plots and partial charge data. In LMFO, e_g electrons are more itinerant than the t_{2g} electrons and therefore repulsion U has a smaller impact on them. This leads to a smaller energy splitting between up- and down-spin states of e_g electrons and in turn to positioning of e_g states between t_{2g} states.

corresponds to their position in the DOS. Assuming that the electronic configuration of Mn is $3d^3_\uparrow d^0_\downarrow$, then the O-$p_\uparrow$ electron has a higher hopping amplitude to Mn-$e_g^\uparrow$ states than the O-$p_\downarrow$ electron because Hund's coupling between t_{2g} and e_g states of Mn favors parallel alignment. On the other hand, the t_{2g} states of Ni are fully occupied. The extra two electrons reside in e_g states and have parallel spins due to Hund's coupling. Since O-$p_\downarrow$ contributes in a superexchange mechanism with the e_g states of Ni, a spin-up configuration is preferred for Ni-e_g electrons. This explains why La_2MnNiO_6 is a ferromagnet. It is worth noting that the alternative Mn^{3+} and Ni^{3+} oxidation states would have led to a AFM configuration, but it is not energetically favorable due to the large crystal-field splitting on Mn ions (see Sec. III).

GGA and GGA + U calculations performed on LMCO lead to similar results. Figures 2(b) and 2(e) show the partial DOS of LMCO. The charge gap is very small in GGA, around 0.1 eV. Adding U splits the Co-t_{2g} states and enhances the charge gap to $\simeq$1.3 eV. Both types of calculations predict a ferromagnetic insulating ground state with $\simeq 6\mu_B$/f.u., which is in agreement with the experimental data [10]. The energy difference between AFM and FM configurations is 0.14 eV/f.u. in GGA calculations and 0.18 eV/f.u. in GGA + U calculations. The superexchange mechanism in LMCO is similar to the one described for LMNO, with the difference that Co has a $3d^5_\uparrow d^2_\downarrow$ electronic configuration [see Fig. 2(h)]. Similarly to LMNO, properties such as charge occupation or partial moments of Mn and Co atoms do not vary sensibly between GGA and GGA + U calculations.

By investigating LMNO and LMCO, we identify a key player in promoting the FM ground state: it is the Mn^{4+} oxidation with three electrons in t_{2g} states that allows the Hund's coupling to become effective and to reduce the total energy of FM state with respect to AFM state.

C. La_2MnFeO_6

In light of the previous results, we move to the interesting case of LMFO. The GGA calculations predict a metallic ferromagnetic ground state for LMFO with finite Fe-d spectral weight at the Fermi level as seen from the density of states of Fig. 2(c). The total moment predicted by GGA calculations is $\sim 7\mu_B$/f.u., which corresponds to high-spin Mn^{4+} and Fe^{2+} states. The energy difference between the AFM and the FM configurations is 0.09 eV/f.u. These results are not in agreement with the available experimental data. Indeed, experiments on high-order films (B-site order $\simeq 63\%$) have found LMFO to be an insulating ferrimagnet with a total moment of $1.3\mu_B$/f.u. and a band gap of 1.1 eV [6]. Adding electron-electron interaction in Fe-d and Mn-d orbitals in the GGA + U framework splits the spectral weight to lower and upper Hubbard bands and opens a spectral gap as shown in Fig. 2(f). Moreover, GGA + U calculations predict an AFM ground state with antiparallel alignment of the moments on Mn and Fe sites and Mn^{3+} and Fe^{3+} states. The energy of the FM configuration is 0.11 eV/f.u. higher than the energy of the AFM configuration. The relaxed structure shows Jahn-Teller distortion due to the presence of Mn^{3+} ions. The predicted magnetic moment is $1\mu_B$/f.u., which is in agreement with $1.3\mu_B$ obtained in experiment for high-order films [6]. The band gap is around 0.2 eV, which is smaller than the experimental band gap 1.1 eV. However, as one can see from Fig. 2(f), the immediate spectral weights around the Fermi level are small, leading to a vanishingly small optical response for photon frequencies causing a transition between them. Therefore, the optical gap measured in experiment appears to be larger than what is calculated. Alternatively, the electron-electron interactions can be stronger than what we have considered here. By comparing calculated optical absorption edge with a measured one, we conclude that $U = 3$ eV is a good approximation. The spectral weight above the Fermi level is predominantly given by Mn-t_{2g}, Fe-e_g, and Fe-t_{2g} which is in agreement with the experimentally obtained spectra [6]. Experimentally, B-site order tends to appear in $A_2B'B''O_6$ double perovskites when the ions on B' and B'' sites have a charge difference larger than 2 and an ionic radius difference larger than 0.17 Å [9]. The GGA + U predicted charges Mn^{3+} and Fe^{3+} could explain why no experiment has reported perfectly ordered LMFO.

One can note that electron-electron interactions in the magnetic ions d shells have a crucial impact on the ground state in LMFO, which is not the case for LMNO or LMCO. The oxidation state for Fe goes from 2^+ (d^6) in GGA calculations to 3^+ (d^5) in GGA + U calculations for the AFM phase. Hence, strong electron-electron interactions prevent double occupancy in Fe-d shells. Moreover, using a larger value of $U_{eff} = 6$ eV in both magnetic ions d shells stabilizes the AFM ground state by further increasing the ground-state total-energy difference between FM and AFM phases.

A simple picture of the superexchange mechanism in LMFO can help understand its AFM ground state. Let us assume that Mn attains 4^+ oxidation state in La_2MnFeO_6, as is the case in LMNO. This oxidation state for Mn requires 2^+ oxidation state for Fe with a $3d_\sigma^5 d_{\bar{\sigma}}^1$ electronic configuration, where one of the Fe-d orbitals is doubly occupied. Such a double occupancy costs a large amount of energy for the system. Hence, the system avoids this energy cost by selecting Mn^{3+} and Fe^{3+} oxidation states if the potential energy cost due to double occupancy of one Fe-d orbital is larger than crystal-field splitting of Mn states. The Mn^{3+} ion has a $3d_\sigma^4 d_{\bar{\sigma}}^0$ electronic configuration with half-filled t_{2g} and one electron in the doubly degenerate e_g states, as illustrated schematically in Fig. 2(i). This electron resides on d_{z^2} state rather than $d_{x^2-y^2}$ state to experience less Coulomb repulsion of O-p electron. This leads to a subsequent Jahn-Teller distortion which lifts the e_g state degeneracy. Therefore, the Mn^{3+} oxidation state and the ensuing Jahn-Teller distortion can be seen as a consequence of the electron-electron interaction on the Fe ions.

The Mn^{3+} and Fe^{3+} oxidation states and the Jahn-Teller distortion set the stage for AFM. If we assume the half-filled Fe-d shell has down spin, then it contributes in a superexchange interaction with the O-$p_\uparrow$ state since the Pauli principle prevents an extra down electron on Fe. The O-$p_\downarrow$ state, on the other hand, contributes in a superexchange interaction with Mn inducing a spin-up configuration for Mn as shown in Fig. 2(i). Therefore, magnetic moments on Mn and Fe align antiparallel leading to a ferrimagnetic ground state for La_2MnFeO_6.

As mentioned above, the Jahn-Teller distortion and other structural distortions play a role in promoting the ferrimagnetic ground state. In $A_2B'B''O_6$ double perovskites, magnetic ions at B' and B'' sites are surrounded by oxygen ions in an octahedral environment. The oxygen octahedra can experience more or less tilting, depending on the ionic radius of the cations at A, B', and B'' sites. Octahedral tiltings lead to B'-O-B'' bonding angles that can differ from the ideal, cubic 180° case [9]. In the relaxed structures, the Mn-O-Fe bonding angles are $\simeq$155° in the FM phase, and $\simeq$153° in the AFM phase. In order to study the impact of structural distortion on the ground state, we generated structures with Mn-O-Fe bonding angles ranging from 150° to 180°. We also studied structures with and without imposing Jahn-Teller distortion. Above $\simeq$165°, the ground state is ferromagnetic without Jahn-Teller distortion. The oxidation states are Mn^{4+} and Fe^{2+}. Below $\simeq$165°, as in the case of the relaxed structure, the ground state is antiferromagnetic with Jahn-Teller distortion. The oxidation states are Mn^{3+} and Fe^{3+}. In the absence of Jahn-Teller distortion, the unoccupied Mn-e_g state has a higher overlap with O-$p_\uparrow$ state, opening a hopping channel for this electron. In that case, O-$p_\downarrow$ can hop to Fe if the five d orbitals are occupied by up instead of down electrons. This spin configuration decreases the total energy of the FM configuration with spin-up Mn. This is confirmed by our *ab initio* calculations without Jahn-Teller distortion.

From the above discussion, one can see that ideal situation for a FM ground state in the 3d-3d double-perovskite oxides occurs when transition metals have d^3-d^8 configuration which happens in LMNO. This explains why LMNO has the largest Curie temperature $T_C = 280$ K in this family.

III. MAGNETIC EXCHANGE COUPLINGS AND CURIE TEMPERATURE

Another important factor in designing magnetocaloric materials is the Curie temperature T_C. Estimating T_C from

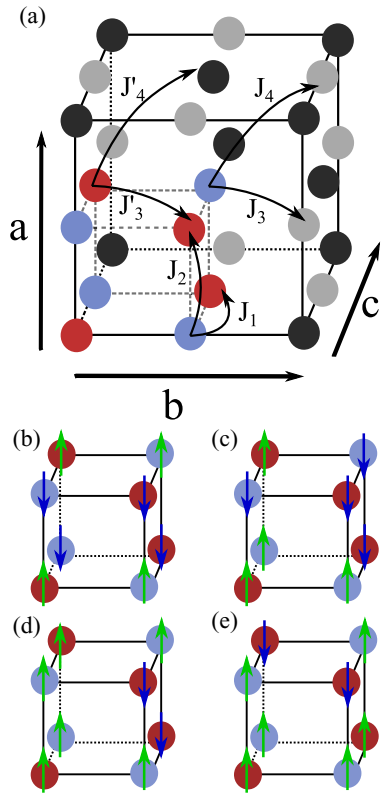

FIG. 3. Top panel: (a) reduced supercell with the four nonequivalent Mn (blue) and Ni(Co, Fe) (red) atoms. The gray atoms are on the Mn sublattice and the black ones on the Ni(Co, Fe) sublattice. The lattice vector **a** denotes the out-of-plane direction, while the lattice vectors **b** and **c** generate the plane. Bottom panel: spin configuration for Mn (blue) and Ni(Co, Fe) (red) sublattices in (b) AFM4, (c) AFM5, (d) AFM6, and (e) FiM phases.

ab initio calculations is a challenging task. One approximate way, which we follow here, is to derive a spin Hamiltonian for the system and then evaluate its transition temperature. In the following subsection, we present the method. The results follow.

A. Extracting the exchange constants

We neglect the induced magnetic moment of oxygen because it is very small in comparison to magnetic moments of the transition-metal ions. The magnetic exchange interaction can be evaluated by mapping the DFT total energy to the Ising model [15]

$$H = -\sum_{ij} J_{ij} S_i^z S_j^z, \tag{1}$$

where J_{ij} is the exchange interaction between spins S_i^z and S_j^z residing at the ith and jth sites, respectively. Here, we assume that the exchange couplings have energy units, hence, the spin values are divided by the Bohr magneton. To obtain the long-range exchange interactions, we first consider a $2 \times 2 \times 2$ supercell. The primitive unit cell contains two Mn ions and two Ni(Co, Fe) ions, hence, the supercell contains 32 magnetic ions. We consider six independent exchange pathways connecting various Mn and Ni(Co, Fe) sites. J_1 and J_2 are the nearest-neighbor in-plane and out-of-plane couplings between Mn and Ni(Fe, Co), while $J_3(J_3')$ and $J_4(J_4')$ are the next nearest-neighbor in-plane and out-of-plane couplings between Mn(Ni, Fe, Co) magnetic moments. The exchange couplings are illustrated in Fig. 3(a).

TABLE I. Spin configuration of the sublattices used in the eight magnetic configurations. The transition-metal sublattice spin configurations are (i) in-plane and out-of-plane FM, (ii) in-plane FM and out-of-plane AFM, and (iii) in-plane AFM and out-of-plane FM. For AFM4, the spin alignment of the sublattices is chosen in such a way that the out-of-plane nearest-neighbor alignment is AFM. Spin alignment of the sublattices in configurations AFM5, AFM6, and FiM does not influence the expression of the total energy since there is no net contribution of nearest-neighbor (Mn-Fe/Co/Ni) interaction to the total energy. Uncommon configurations AFM4, AFM5, FiM, and AFM6 are illustrated in Figs. 3(b)–3(e).

Configuration	Sublattice B' Mn	Sublattice B'' Ni, Co, Fe	Spin alignment
FM	i	i	in phase
AFM1 (G-type)	i	i	out of phase
AFM2 (A-type)	ii	ii	in phase
AFM3 (C-type)	ii	ii	out of phase
AFM4	iii	iii	(see caption)
AFM5	ii	iii	n.a.
FiM	i	ii	n.a.
AFM6	i	iii	n.a.

In order to reduce the errors, we work with the total-energy differences with respect to the ground state rather than the absolute total-energy values. We fixed the structure and changed the magnetic order between eight different spin configurations and calculated their total energy. The spin configurations are chosen by adopting different configurations for each transition-metal sublattice. Each sublattice can have the following spin configurations: (i) in-plane and out-of-plane FM, (ii) in-plane FM and out-of-plane AFM, (iii) in-plane AFM and out-of-plane FM. The chosen spin configurations are given in Table I. Because of symmetries common to all the magnetic orders considered in the calculations, we were able to reduce the $2 \times 2 \times 2$ supercells to smaller ones that are twice as big as the primitive ones. These reduced supercells contain four nonequivalent Mn and four nonequivalent Ni(Fe, Co) atoms, hence, a total of eight magnetic ions.

We use GGA calculations to find the energy of each configuration in the LMNO and LMCO phases. In the case of LMFO, since GGA does not predict the right ground state, we use GGA + U with $U_{eff} = 3.0$ eV in Mn-3d and Fe-3d shells to find the energies.

The corresponding total energy mapped to the Ising model can be obtained as follows. The primitive unit cell contains two Mn and two Ni (Co, Fe) ions. Each Mn (Ni, Co, Fe) has four in-plane and two out-of-plane nearest neighbors which belong to the other sublattice. The number of in-plane and out-of-plane next-nearest neighbors are eight and four, respectively, and they belong to the same sublattice. Therefore, letting S^z and S'^z denote the z component of the spin on B' and B'' sublattices, the nearest-neighbor interaction contributes $-4J_1 S^z S'^z - 2J_2 S^z S'^z$ per magnetic ion to the total energy

TABLE II. Calculated magnetic exchange interactions for LMNO, LMCO, and LMFO. Positive (negative) value denotes FM (AFM) coupling. The extreme values of the spins are $\mathcal{S}^z_{\mathrm{Mn}} = \frac{3}{2}$, $\mathcal{S}'^z_{\mathrm{Ni}} = 1$, $\mathcal{S}'^z_{\mathrm{Co}} = \frac{3}{2}$ in LMNO and LMCO, and $\mathcal{S}^z_{\mathrm{Mn}} = 2$ and $\mathcal{S}'^z_{\mathrm{Fe}} = \frac{5}{2}$ in LMFO.

		Values (meV)		
	Interaction path	LMNO	LMCO	LMFO
J_1	Mn-B'' (in plane)	4.51	3.36	− 1.75
J_2	Mn-B'' (out of plane)	4.09	2.85	− 0.97
J_3	Mn-Mn (in plane)	− 0.15	− 0.59	− 0.04
J_4	Mn-Mn (out of plane)	− 0.10	− 0.45	− 0.28
J'_3	B''-B'' (in plane)	− 0.04	0.28	0.16
J'_4	B''-B'' (out of plane)	− 0.11	0.08	− 0.18

while the next-nearest-neighbor interaction contribution depends on the sublattice and is given by $-4J_3\mathcal{S}^z S^z - 8J_4\mathcal{S}^z\mathcal{S}^z$ or $-4J'_3S'^zS'^z - 8J'_4S'^zS'^z$ per magnetic ion. Therefore, the total energies of the above spin configurations for primitive unit cell are

$$E^{\mathrm{FM}}_{\mathrm{tot}} = -(16J_1 + 8J_2)\mathcal{S}^z\mathcal{S}'^z - (8J_3 + 16J_4)\mathcal{S}^{z2} - (8J'_3 + 16J'_4)\mathcal{S}'^{z2}, \quad (2)$$

$$E^{\mathrm{AFM1}}_{\mathrm{tot}} = +(16J_1 + 8J_2)\mathcal{S}^z\mathcal{S}'^z - (8J_3 + 16J_4)\mathcal{S}^{z2} - (8J'_3 + 16J'_4)\mathcal{S}'^{z2}, \quad (3)$$

$$E^{\mathrm{AFM2}}_{\mathrm{tot}} = -(16J_1 - 8J_2)\mathcal{S}^z\mathcal{S}'^z - (8J_3 - 16J_4)\mathcal{S}^{z2} - (8J'_3 - 16J'_4)\mathcal{S}'^{z2}, \quad (4)$$

$$E^{\mathrm{AFM3}}_{\mathrm{tot}} = +(16J_1 - 8J_2)\mathcal{S}^z\mathcal{S}'^z - (8J_3 - 16J_4)\mathcal{S}^{z2} - (8J'_3 - 16J'_4)\mathcal{S}'^{z2}, \quad (5)$$

$$E^{\mathrm{AFM4}}_{\mathrm{tot}} = +8J_2\mathcal{S}^z\mathcal{S}'^z + 8J_3S^{z2} + 8J'_3S'^{z2}, \quad (6)$$

$$E^{\mathrm{AFM5}}_{\mathrm{tot}} = -(8J_3 - 16J_4)\mathcal{S}^{z2} + 8J'_3\mathcal{S}'^{z2}, \quad (7)$$

$$E^{\mathrm{FiM}}_{\mathrm{tot}} = -(8J_3 + 16J_4)\mathcal{S}^{z2} - (8J'_3 - 16J'_4)\mathcal{S}'^{z2}, \quad (8)$$

$$E^{\mathrm{AFM6}}_{\mathrm{tot}} = -(8J_3 + 16J_4)\mathcal{S}^{z2} + 8J'_3\mathcal{S}'^{z2}, \quad (9)$$

where $\mathcal{S}^z$ and $\mathcal{S}'^z$ denote the extreme values of the spins. These equations should be multiplied by 2 to obtain the total energy of the supercell considered here. They yield seven energy differences; six of them are used to calculate the exchange couplings and the last one is used to verify their validity.

B. Calculated exchange constants and mean field Curie temperatures

The calculated magnetic exchange interactions for LMNO are presented in Table II. The nearest-neighbor exchange couplings are FM type and sizable while the next-nearest-neighbor magnetic moments are coupled antiferromagnetically. The rather short-range magnetic interaction is a consequence of the rather localized $3d$ electron wave functions.

TABLE III. Magnetic phase transition temperature in Kelvin obtained from different methods for LMB''O.

	Transition temperature (K)		
	Mean field	Monte Carlo	Experiment
LMNO	527	419	280 [2]
LMCO	505	399	226 [3]
LMFO	418	329	

The next-nearest neighbors are identical ions with half-filled shells and their AFM coupling can be understood in terms of a simple Hubbard model: The AFM alignment of the magnetic moment allows for hopping of the electron between these sites and reduces kinetic energy.

The exchange couplings for LMCO are also listed in Table II. One can notice that the Mn-Co couplings are smaller than the Mn-Ni ones, which is in agreement with the discussion of the superexchange mechanism in these materials of Secs. II B and II C. We argued that, due to the superexchange interaction, the ideal situation to promote an FM phase over an AFM one in the family of compounds studied is the $3d^3$-$3d^8$ case. This situation occurs in LMNO and it could explain why the exchange couplings are larger in this material, and also why its experimental T_C is the largest in this family even though its total moment is not the largest. Once again, the next-nearest-neighbor couplings are smaller than J_1 and J_2 by one or two orders of magnitude due to the localization of $3d$ wave functions. Note that Co-Co exchange couplings are FM. In contrast with LMNO, in which direct hopping between Ni ions only occurs between e_g states, in LMCO the direct hopping processes between t_{2g} states are allowed as well. Hence, a simple argument based on half-filled Hubbard model is not applicable to Co ions.

In the case of LMFO, Mn and Fe magnetic moments are coupled antiferromagnetically, with $|J_1|$ and $|J_2|$ smaller than what we found previously for LMNO and LMCO. Finally, the Curie temperatures evaluated from a mean field treatment of the Ising model are given in Table III. For the details of the mean field calculation, see Appendix A. The mean field theory overestimates the Curie temperatures. However, it gives the correct trend.

Finally, in order to examine the accuracy of the exchange couplings, we used them to evaluate the energy differences of a new magnetic configuration with respect to FM state and compare the results with those found directly from the *ab initio* calculations. The configuration AFM6, given in Table I, was not used in the calculation of the couplings. The energy difference from the *ab initio* calculations and from the Ising model using exchange couplings from Table II are listed in Table IV. The agreement is very good in the case of LMNO (less than 1% of disparity), and relatively good in the cases of LMCO and LMFO (respectively, 5% and 11% of disparity).

IV. TRANSITION TEMPERATURE FROM MONTE CARLO CALCULATIONS

The mean field treatment of the spin Hamiltonian does not take into account fluctuations, hence, overestimates the Curie

TABLE IV. Energy difference between AFM6 phase and FM phase in eV.

	E_{AFM6}-E_{FM}	
	From J values	From *ab initio* calculations
LMNO	0.154	0.155
LMCO	0.176	0.185
LMFO	−0.181	−0.202

temperatures T_C. In order to get better approximations, we perform classical Monte Carlo calculations with the GT-GPU method on a cubic lattice [16] using the J and extreme spin values listed in Table II.

A. Monte Carlo methodology

Genetic tempering is a Monte Carlo algorithm that uses many copies of the Metropolis-Hastings algorithm [17–19] to generate highly precise statistical measurements and eliminate autocorrelation error. To ensure accuracy, initial state samples are chosen from unconverged samples surrounding the target answer. Running another round of Monte Carlo sampling on these initial states gives a partial cancellation of the relaxation error.[1] The T_C is obtained from Binder's cumulant [19] $B(T, L) = 1 - \langle M^4\rangle_L/(3\langle M^2\rangle_L^2)$, with L the linear lattice size. In the thermodynamic limit $L \to \infty$, the Binder's cumulant tends towards $\frac{2}{3}$ for $T < T_C$ and 0 for $T > T_C$, hence, it is discontinuous in this limit. In simulation with finite L, the intersection point of the Binder's cumulants for different system sizes determines T_C and usually depends only rather weakly on those sizes.

B. Improved Curie temperatures

The Curie temperatures obtained from Monte Carlo are shown in Table III and compared with mean-field values and experimental ones. The transition temperature of bulk ordered LMFO is not known but the magnetization measurements indicate a lower T_C than LMCO, as seen in Fig. 1. As can be seen from Table III, both mean field and Monte Carlo give consistent trend with experimental data but overestimate them. The Monte Carlo prediction is closer to experimental transition temperatures. It is worth mentioning that Curie temperature of LMNO and LMCO are affected by the (AF) next-nearest-neighbor exchange coupling: they have smaller magnitude in comparison with nearest-neighbor exchange coupling, but the number of next-nearest neighbor is larger. Finally, capturing the correct trend allows both mean field and Monte Carlo methods to be used reliably in material design.

[1]Here, 10^5 uncounted steps and 5×10^3 counted steps were used in initial state samples, while 5×10^5 uncounted steps with 10^6 counted steps were used in calculating the Binder's cumulant. Random numbers were made with the counter-based random number generator of Ref. [21]. All data for a single system size were obtained with one graphics processing unit and one computing processing unit in 1–2 hours or less.

V. CONCLUDING REMARKS

We used GGA and GGA + U calculations in order to understand the ground-state electronic and magnetic properties of double perovskite La_2MnFeO_6. This material is predicted to be an insulating ferrimagnet, unlike similar compounds La_2MnCoO_6 and La_2MnNiO_6, which are insulating ferromagnets. This study helped us understand the important role played by electron-electron interactions in the determination of the ground state of this material. We also showed that the interplay between crystal field, Mn-O-Fe bonding angle, and electron-electron interactions also needs to be taken into consideration when analyzing the superexchange mechanism in LMFO.

Large electron-electron interactions in Fe-3d shells promote Mn^{3+} and Fe^{3+} oxidation states and AFM ground state in LMFO. In contrast, we also saw that Mn-O-Fe bonding angles superior to $\simeq 165^\circ$ promote a FM ground state with Mn^{4+} and Fe^{2+} oxidation states. From these observations, we believe that studying two different new materials could be of interest in the global topic of magnetic refrigeration.

First, in order to avoid the strong electronic repulsion in 3d shells that promote an AFM ground state in LMFO over an FM one, one could study the double perovskite La_2MnRuO_6 (LMRO). Valence orbitals in Ru are 4d, which are more extended in space than Fe-3d orbitals. Smaller correlations in LMRO could lead to a FM ground state with Mn^{4+} and Ru^{2+} oxidation states. However, experiments on disordered LMRO (space group $Pnma$) have found this material to be a ferrimagnet with trivalent Mn in high-spin configuration and trivalent Ru in low-spin configuration [20]. The effect of the ordering of Mn and Ru atoms still needs to be investigated.

The second option is to get rid of an excess electron in Fe by hole doping the compound, which could lead to Mn^{4+} and Fe^{3+} oxidation states. If both Mn and Fe are in high-spin configuration, these oxidation states would lead to a ferromagnetic superexchange interaction. Moreover, the substitution of La^{3+} cations with larger divalent cations would increase the tolerance factor of the material, which would in turn reduce the amount of octahedral tilting. This avenue will be explored further in work to come.

ACKNOWLEDGMENTS

We are indebted to M. Côté for numerous discussions. This work has been supported by the Natural Sciences and Engineering Research Council of Canada (NSERC) under Grant No. RGPIN-2014-04584, by the Canada First Research Excellence Fund, and by the Research Chair in the Theory of Quantum Materials. T.E.B. graciously thanks funding provided by the postdoctoral fellowship from Institut quantique. T.E.B. thanks Y. Liu, G. Evenbly, and D. Poulin for discussions. *Ab initio* simulations and Monte Carlo calculations were performed on computers provided by the Canadian Foundation for Innovation, the Ministère de l'Éducation des Loisirs et du Sport (Québec), Calcul Québec, Compute Canada and the Fonds de recherche du Québec-Nature et technologies (FRQNT).

APPENDIX: MEAN FIELD THEORY FOR CURIE TEMPERATURE

In this appendix we recall mean field theory for double perovskites, which allows us to estimate the Curie temperature. The magnetic system of LMNO, LMCO, and LMFO can be modeled by the Ising model (1). The mean field approximation is to replace the configurational energy by the energy of a noninteracting system of spins each experiencing a field h_{MF}. The mean field Hamiltonian can be obtained by substituting $S_i^z = \langle S_i^z\rangle + \delta S_i^z$ with $\delta S_i^z \equiv S_i^z - \langle S_i^z\rangle$ and neglecting terms of order $(\delta S_i^z)^2$ in Eq. (1). For the FM configuration, the mean field energy is

$$E_{\mathrm{MF}}^{\mathrm{FM}} = -\sum_i h_{\mathrm{MF}} S_i^z - \sum_j h'_{\mathrm{MF}} S_j'^z, \tag{A1}$$

$$h_{\mathrm{MF}} = 2(4J_1 + 2J_2)m' + 2(4J_3 + 8J_4)m, \tag{A2}$$

$$h'_{\mathrm{MF}} = 2(4J_1 + 2J_2)m + 2(4J'_3 + 8J'_4)m', \tag{A3}$$

where magnetizations per spin are $m = (1/2N)\sum_i \langle S_i^z\rangle$ and $m' = (1/2N)\sum_i \langle S_i'^z\rangle$ and $2N$ denotes the total number of sites of a given type. Recall that h_{MF} and h'_{MF} depend on temperature through the temperature dependence of m and m'.

The magnetization per spin is given by $m = \sum_{S_i^z} p(S_i^z) S_i^z$ where $p(S_i^z)$ denotes the single-spin Boltzmann distribution

$$p\left(S_i^z\right) = \left(\frac{1}{\mathcal{Z}}\right) \exp\left(\beta h_{\mathrm{MF}} S_i^z\right), \tag{A4}$$

and $\mathcal{Z}$ is the partition function

$$\mathcal{Z} = ZZ' = \sum_{S_i^z} \exp\left(\beta h_{\mathrm{MF}} S_i^z\right) \sum_{S_i'^z} \exp\left(\beta h'_{\mathrm{MF}} S_i'^z\right). \tag{A5}$$

It is straightforward to show that the magnetizations are given by Brillouin functions

$$m(T) = \frac{1}{\beta}\frac{\partial \ln(Z)}{\partial h_{\mathrm{MF}}} = -\frac{1}{2}\coth(\beta h_{\mathrm{MF}}/2) + \left(\mathcal{S}^z + \frac{1}{2}\right)\coth[\beta h_{\mathrm{MF}}(\mathcal{S}^z + 1/2)], \tag{A6}$$

$$m'(T) = \frac{1}{\beta}\frac{\partial \ln(Z')}{\partial h'_{\mathrm{MF}}} = -\frac{1}{2}\coth(\beta h'_{\mathrm{MF}}/2) + \left(\mathcal{S}'^z + \frac{1}{2}\right)\coth[\beta h'_{\mathrm{MF}}(\mathcal{S}'^z + 1/2)], \tag{A7}$$

where $\mathcal{S}^z$ and $\mathcal{S}'^z$ denote the extreme values of the spins. For example, for LMNO, they are $\mathcal{S}^z_{\mathrm{Mn}} = \frac{3}{2}$ and $\mathcal{S}'^z_{\mathrm{Ni}} = 1$. Note that one could have used $\mathcal{S}^z_{\mathrm{Mn}} = 3$ and $\mathcal{S}'^z_{\mathrm{Ni}} = 2$ which renormalizes the exchange couplings but leaves Curie temperature invariant. These coupled equations can be solved to obtain m and m'. For high T (low β), the only solution is $m = m' = 0$ whereas for low T there are possible nontrivial solutions. The solution with nonzero $|m|$ and $|m'|$ appears at Curie temperature. By expanding the coth functions in the limit of small h_{MF} and h'_{MF}, the above equations give the eigenvalue problem

$$m(T) = \frac{\mathcal{S}^z(\mathcal{S}^z + 1)}{3k_B T} h_{\mathrm{MF}}(T), \tag{A8}$$

$$m'(T) = \frac{\mathcal{S}'^z(\mathcal{S}'^z + 1)}{3k_B T} h'_{\mathrm{MF}}(T), \tag{A9}$$

which yields the following equation for Curie temperature:

$$3k_B T_C = [\mathcal{S}^z(\mathcal{S}^z + 1)h_2 + \mathcal{S}'^z(\mathcal{S}'^z + 1)h'_2] + \sqrt{4h_1^2 \mathcal{S}^z(\mathcal{S}^z + 1)\mathcal{S}'^z(\mathcal{S}'^z + 1) + [\mathcal{S}^z(\mathcal{S}^z + 1)h_2 - \mathcal{S}'^z(\mathcal{S}'^z + 1)h'_2]^2}, \tag{A10}$$

where we have defined $h_1 = 4J_1 + 2J_2$, $h_2 = 4J_3 + 8J_4$, and $h'_2 = 4J'_3 + 8J'_4$. Note that in the case with identical moments $\mathcal{S}^z = \mathcal{S}'^z$ and only nearest-neighbor coupling, the above equation reduces to textbook formula, i.e., $3k_B T_C = 2h_1 \mathcal{S}^z(\mathcal{S}^z + 1)$.

Assuming that LMFO undergoes a ferrimagnetic to paramagnetic transition at Néel temperature T_N, then T_N can also be obtained from (A10). In this case, the only difference between the treatment of T_N and T_C is the sign of nearest-neighbor interaction h_1, which also appears in h_{MF} and h'_{MF}. However, the sign of h_1 disappears in (A10). For the classical Ising model on bipartite lattices, it is well known that a simple relabeling of up and down for one of the sublattices maps the nearest-neighbor ferromagnetic model to the antiferromagnetic one.

[1] J. R. Gómez, R. F. Garcia, A. D. M. Catoira, and M. R. Gómez, Renewable Sustainable Energy Rev. **17**, 74 (2013).

[2] N. Rogado, J. Li, A. Sleight, and M. Subramanian, Adv. Mater. **17**, 2225 (2005).

[3] R. I. Dass and J. B. Goodenough, Phys. Rev. B **67**, 014401 (2003).

[4] M. Balli, P. Fournier, S. Jandl, and M. M. Gospodinov, J. Appl. Phys. **115**, 173904 (2014).

[5] M. Hashisaka, D. Kan, A. Masuno, M. Takano, Y. Shimakawa, T. Terashima, and K. Mibu, Appl. Phys. Lett. **89**, 032504 (2006).

[6] K. Yoshimatsu, K. Nogami, K. Watarai, K. Horiba, H. Kumigashira, O. Sakata, T. Oshima, and A. Ohtomo, Phys. Rev. B **91**, 054421 (2015).

[7] K. Ueda, H. Tabata, and T. Kawai, Phys. Rev. B **60**, R12561 (1999).

[8] K. Ueda, Y. Muraoka, H. Tabata, and T. Kawai, Appl. Phys. Lett. **78**, 512 (2001).

[9] S. Vasala and M. Karppinen, Prog. Solid State Chem. **43**, 1 (2015).

[10] M. Balli, P. Fournier, S. Jandl, K. D. Truong, and M. M. Gospodinov, J. Appl. Phys. **116**, 073907 (2014).

[11] J. Pezhumkattil Palakkal, P. N. Lekshmi, S. Thomas, K. G. Suresh, and M. R. Varma, RSC Adv. **5**, 105531 (2015).

[12] M. P. Singh, K. D. Truong, S. Jandl, and P. Fournier, Phys. Rev. B **79**, 224421 (2009).

[13] P. Blaha, K. Schwarz, G. K. H. Madsen, D. Kvasnicka, and J. Luitz, *WIEN2K, An Augmented Plane Wave + Local Orbitals Program for Calculating Crystal Properties* (Karlheinz Schwarz, Techn. Universität Wien, Austria, 2001).

[14] V. I. Anisimov, I. V. Solovyev, M. A. Korotin, M. T. Czyżyk, and G. A. Sawatzky, Phys. Rev. B **48**, 16929 (1993).

[15] S. Kanungo, B. Yan, M. Jansen, and C. Felser, Phys. Rev. B **89**, 214414 (2014).

[16] T. E. Baker, arXiv:1801.09379.

[17] N. Metropolis, A. W. Rosenbluth, M. N. Rosenbluth, A. H. Teller, and E. Teller, J. Chem. Phys. **21**, 1087 (1953).

[18] W. K. Hastings, Biometrika **57**, 97 (1970).

[19] D. P. Landau and K. Binder, *A Guide to Monte Carlo Simulations in Statistical Physics* (Cambridge University Press, Cambridge, 2014).

[20] N. Kamegashira, T. Mori, A. Imamura, and Y. Hinatsu, J. Alloys Compd. **302**, L6 (2000).

[21] J. K. Salmon, M. A. Moraes, R. O. Dror, and D. E. Shaw, *High Performance Computing, Networking, Storage and Analysis (SC), 2011 IEEE International Conference* (IEEE, Piscataway, NJ, 2011), pp. 1–12.